

# Vascular Anatomy-aware Self-supervised Pre-training for X-ray Angiogram Analysis

De-Xing Huang, Chaohui Yu, Xiao-Hu Zhou, *Member, IEEE*, Tian-Yu Xiang, Qin-Yi Zhang, Mei-Jiang Gui, Rui-Ze Ma, Chen-Yu Wang, Nu-Fang Xiao, Fan Wang, and Zeng-Guang Hou, *Fellow, IEEE*

**Abstract**— X-ray angiography is the gold standard imaging modality for cardiovascular diseases. However, current deep learning approaches for X-ray angiogram analysis are severely constrained by the scarcity of annotated data. While large-scale self-supervised learning (SSL) has emerged as a promising solution, its potential in this domain remains largely unexplored, primarily due to the lack of *effective SSL frameworks* and *large-scale datasets*. To bridge this gap, we introduce a Vascular anatomy-aware Masked Image Modeling (VasoMIM) framework that explicitly integrates domain-specific anatomical knowledge. Specifically, VasoMIM comprises two key designs: an *anatomy-guided masking strategy* and an *anatomical consistency loss*. The former strategically masks vessel-containing patches to compel the model to learn robust vascular semantics, while the latter preserves structural consistency of vessels between original and reconstructed images, enhancing the discriminability of the learned representations. In conjunction with VasoMIM, we curate XA-170K, the largest X-ray angiogram pre-training dataset to date. We validate VasoMIM on four downstream tasks across six datasets, where it demonstrates superior transferability and achieves state-of-the-art performance compared to existing methods. These findings highlight the significant potential of VasoMIM as a foundation model for advancing a wide range of X-ray angiogram analysis tasks. VasoMIM and XA-170K will be available at <https://github.com/Dxhuang-CASIA/XA-SSL>.

This work was supported in part by the National Key Research and Development Program of China under Grant 2023YFC2415100, in part by the National Natural Science Foundation of China under Grant 62373351, Grant 62503474, Grant 82327801, Grant 62303463, in part by the Chinese Academy of Sciences Project for Young Scientists in Basic Research under Grant No. YSBR-104, in part by the Beijing Natural Science Foundation under Grant F252068, Grant 4254107, in part by Beijing Nova Program under Grant 20250484813, in part by China Postdoctoral Science Foundation under Grant 2024M763535, in part by the Postdoctoral Fellowship Program of CPSF under Grant GZC20251170, and in part by Xiaomi Young Talents Program/Xiaomi Foundation. (Corresponding authors: Xiao-Hu Zhou and Zeng-Guang Hou)

D.-X. Huang, X.-H. Zhou, T.-Y. Xiang, Q.-Y. Zhang, M.-J. Gui, R.-Z. Ma, C.-Y. Wang, N.-F. Xiao and Z.-G. Hou are with the State Key Laboratory of Multimodal Artificial Intelligence Systems, Institute of Automation, Chinese Academy of Sciences, Beijing 100190, China (email: [>{huangdexing2022, xiaohu.zhou, zengguang.hou}@ia.ac.cn}](mailto:{huangdexing2022, xiaohu.zhou, zengguang.hou}@ia.ac.cn)).

D.-X. Huang, X.-H. Zhou, T.-Y. Xiang, Q.-Y. Zhang and Z.-G. Hou are also with the School of Artificial Intelligence, University of Chinese Academy of Sciences, Beijing 100049, China.

Z.-G. Hou is also with the Joint Laboratory of Intelligence Science and Technology, Institute of Systems Engineering, Macau University of Science and Technology, Taipa, Macao, China.

C. Yu and F. Wang are with the DAMO Academy, Alibaba Group, Hangzhou 310023, China. C. Yu is also with Hupan Lab, Hangzhou 310023, China.

**Index Terms**— X-ray Angiogram Analysis, Self-supervised Pre-training, Anatomy-aware, Masked Image Modeling.

## I. INTRODUCTION

CARDIOVASCULAR diseases (CVDs) constitute a global health crisis and remain the leading cause of mortality worldwide [1]. X-ray angiography serves as the gold standard for diagnosing CVDs [2], planning interventions [3], and guiding procedures [4]. However, accurate interpretation of these angiograms is fraught with challenges. Radiologists often struggle to precisely delineate vascular topology or identify stenosis due to low contrast, motion artifacts, and overlapping anatomical structures [5]. Consequently, there is an urgent demand for automated, robust image analysis methodologies.

With the advent of artificial intelligence (AI), numerous techniques have been proposed to mitigate clinical workload, ranging from vessel segmentation [5] to stenosis detection [6], [7]. Despite these advances, training high-performance models requires datasets with pixel-level annotations. Producing such annotations is labor-intensive, time-consuming, and dependent on specialized domain knowledge [8]. To address this bottleneck, the community is shifting from supervised training on small datasets to self-supervised learning (SSL), which leverages vast amounts of unlabeled data to learn generalizable representations [9]. Yet, the potential of SSL in this domain remains largely underexplored. This gap can be attributed to two primary hurdles: the lack of *domain-specific SSL frameworks* and the absence of *large-scale datasets*.

As a representative SSL technique, masked image modeling (MIM) has achieved remarkable success in medical image analysis [10]–[12] by training models to reconstruct masked image patches (Fig. 1 (a)). However, the direct application of standard MIM to X-ray angiograms is suboptimal due to the *extreme sparsity of vascular structures*: *i) Anatomically agnostic masking strategies fail to prioritize sparse vessel-relevant regions*. Current strategies rely on generic rules, either data-independent (e.g., random [10], block-wise [13]) or data-adaptive (e.g., attention-based [14] or loss-based [15]). While effective for natural images with dense semantic content, these strategies often ignore thin vascular structures. As illustrated in Fig. 2, standard strategies tend to mask background regions simply because they dominate image statistics, rendering the model insensitive to critical vascular anatomy. *ii) Conventional reconstruction objectives lack semantic*

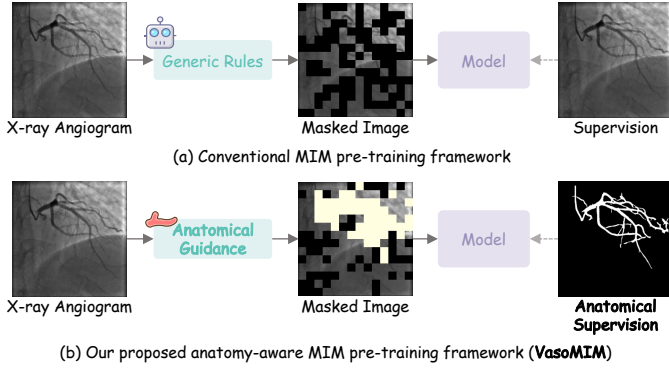


**Fig. 1:** Conceptual comparison. (a) Conventional MIM masks patches based on *generic rules* and utilizes *standard supervision* to reconstruct the original image. (b) VasoMIM employs *anatomical guidance* to selectively mask vessel-relevant regions (highlighted in yellow) and enforces structural consistency via *anatomical supervision*, enabling the model to learn richer vascular representations.

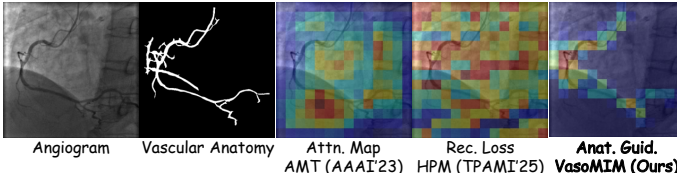


**Fig. 2:** Generic vs. anatomy-guided masking strategies. While generic methods like AMT and HPM fail to prioritize vascular structures, VasoMIM effectively focuses on vessel-relevant regions. Red denotes a higher masking probability, while blue indicates the opposite.

**discriminability.** Existing approaches learn reconstruction via pixel-level regression [10] or feature distillation [16]. Pixel-level loss encourages the prediction of low-frequency background textures rather than high-frequency vascular details. While feature distillation methods [13], [15], attempt to alleviate this, they are computationally expensive and, being pre-trained on natural images, lack domain-specific semantics.

To address these challenges, we introduce **Vascular anatomy-aware Masked Image Modeling (VasoMIM)**, a framework tailored for X-ray angiograms, as presented in Fig. 1 (b). The core insight is to inject a strong anatomical inductive bias into the model. **First, we design an *anatomy-guided masking strategy* that directs the model’s focus toward vessel-relevant regions.** Unlike approaches relying on indirect feedback [14], [15], we utilize vascular anatomy directly extracted via Frangi filter [17] as guidance, forcing the model to learn to reconstruct the most informative regions. **Second, we introduce an *anatomical consistency loss* to enhance representation discriminability.** We enforce consistency between the vascular segmentation of the original and reconstructed images using a lightweight segmentor (UNeXt-S [18], 0.26M), ensuring the model learns topologically accurate representations rather than mere pixel intensities.

Effective pre-training requires data at scale. Unlike other modalities such as CT [19], MRI [20], and chest X-ray [21],

the X-ray angiogram domain lacks established large-scale datasets. To this end, we curate XA-170K, which, to the best of our knowledge, stands as the largest publicly available dataset for X-ray angiogram pre-training.

The main contributions of this study are as follows:

- A novel self-supervised pre-training framework, VasoMIM, is proposed for X-ray angiogram analysis. This method explicitly integrates vascular anatomical knowledge to drive robust vascular representation learning.
- The existing largest X-ray angiogram pre-training dataset, XA-170K, is introduced. Leveraging this dataset, we provide the first empirical verification of scaling laws for MIM in this specific domain.
- Extensive experiments across four downstream tasks and six datasets demonstrate that VasoMIM significantly outperforms state-of-the-art SSL alternatives.

The preliminary version of this study was published at AAAI 2026 [22]. In this extended version, we present substantial new contributions: *i) Scaling-up Data.* We expand the pre-training dataset from 20K to 170K. Crucially, we systematically verify the scaling laws of VasoMIM regarding both data scale and model capacity, providing empirical evidence for the benefits of large-scale pre-training. *ii) Methodological Refinement.* Compared to VasoMIM-v1 [22], which solely used vascular anatomy extracted by Frangi filter as guidance, we further integrate probability maps of the segmentor as co-guidance, reducing the noise interference caused by bony structures. *iii) Comprehensive Verification.* We expand validation from a single task to four distinct clinical applications: vessel segmentation, vessel segment segmentation, stenosis segmentation, and stenosis detection. Furthermore, we include a wider range of state-of-the-art baselines to ensure a rigorous and comprehensive comparison. *iv) In-depth Analysis.* We provide detailed analyses of the core design choices, offering deeper insights into the mechanism of anatomy-aware pre-training.

## II. RELATED WORKS

### A. Self-supervised Medical Image Pre-training

Self-supervised learning (SSL) can learn transferable visual representations without annotations [10], [13], [23]–[25]. It has become a cornerstone for large-scale vision pre-training [9]. State-of-the-art SSL approaches generally fall into two categories: contrastive learning (CL) and masked image modeling (MIM). CL methods [19], [23], [26] aim to align positive pairs while separating negative pairs in the embedding space. While effective for image-level tasks like classification, these methods often struggle with dense prediction tasks [27], such as segmentation and detection, which require fine-grained spatial representations. Conversely, MIM approaches train models to reconstruct masked patches from visible context, enabling the learning of detailed local representations [28]. Generic MIM frameworks like MAE [10] and SimMIM [25] have been successfully adapted to medical imaging, with further enhancements tailored to specific modalities including ultrasound [29], CT [11], fMRI [30], and pathology [31]. To the best of our knowledge, this work presents the first domain-

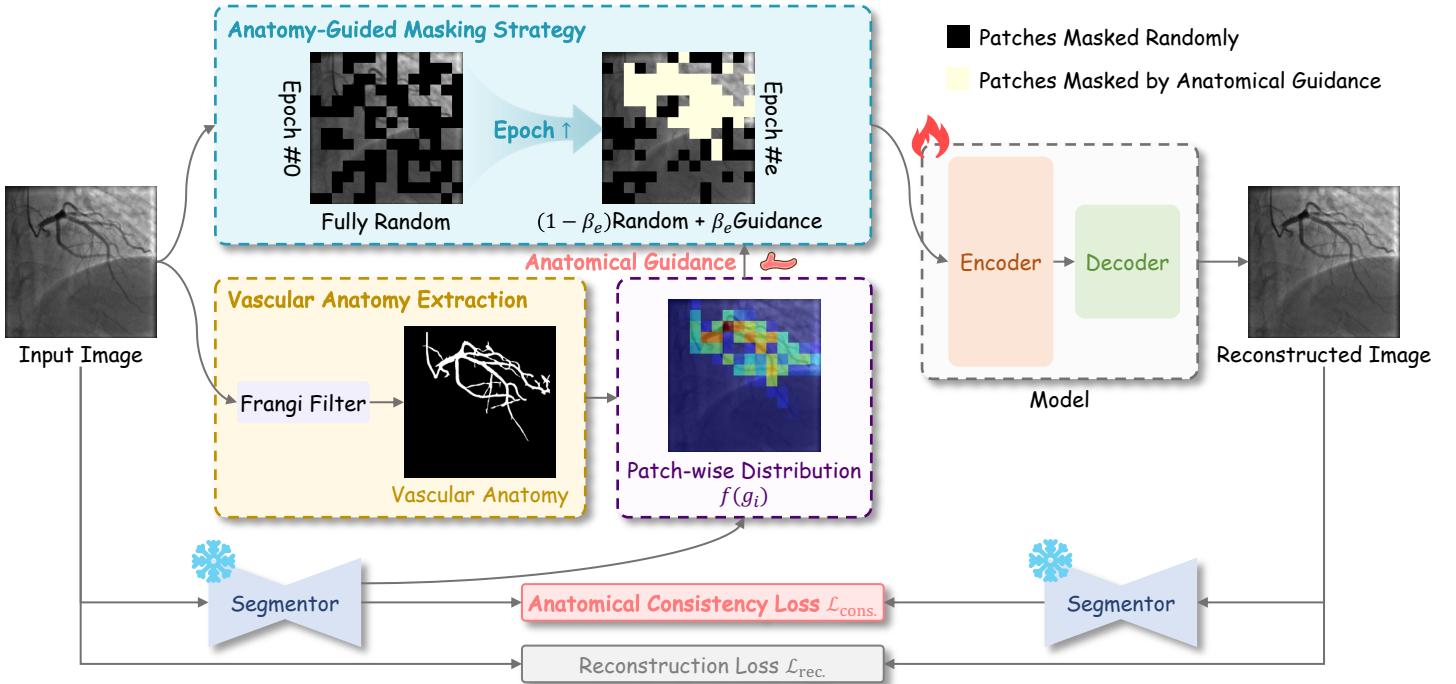


**Fig. 3:** Overview of VasoMIM. First, vascular anatomy is extracted from the input X-ray angiogram via Frangi filter. A patch-wise vascular anatomical distribution  $f(g_i)$  is then computed to guide the masking strategy, prioritizing vessel-relevant regions. Finally, the model is optimized by minimizing the total objective  $\mathcal{L}_{\text{MIM}}$ , which combines the standard pixel-level reconstruction loss  $\mathcal{L}_{\text{rec.}}$  with the proposed anatomical consistency loss  $\mathcal{L}_{\text{cons.}}$  to learn discriminative vascular representations.

specific MIM framework and the largest pre-training dataset for X-ray angiogram analysis.

### B. Two Key Components in MIM

**Masking Strategy.** The efficacy of MIM relies heavily on the masking strategy, particularly given the high spatial redundancy of images [10]. While simple random masking with high ratios is the standard [15], [29], it often fails to isolate the most discriminative regions. To address this, various carefully designed strategies have been proposed: AMT [14] leverages attention maps to guide masking. HAP [28] exploits human-structure priors for human-centric perception. Other approaches, such as HPM [15], AnatoMask [32], and AHM [33], employ loss predictors, self-distillation, or policy networks to identify and mask “hard” patches. Despite their effectiveness in generic scenarios, these methods remain insensitive to the sparse vascular structures in X-ray angiograms due to the extreme dominance of the background, as illustrated in Fig. 2. In contrast, our anatomy-guided masking strategy explicitly directs the model’s focus toward vascular regions using vascular anatomy extracted via Frangi filter.

**Reconstruction Objectives.** MIM trains models to reconstruct masked patches according to pre-defined objectives. The most common approach minimizes mean squared error (MSE) [10] or mean absolute error (MAE) [25] in the raw RGB pixel space. However, pixel-level objectives are highly susceptible to background noise [15], especially in the case that background and vascular pixels are significantly imbalanced. Alternative objectives distill high-level representations

from pre-trained foundation models [13], [15]. While effective for natural images, these models fail to capture the specific anatomical semantics of X-ray angiograms due to the significant domain gap. To bridge this gap, we leverage vascular anatomy extracted via Frangi filter [17] as pseudo-labels to train a lightweight segmentor [18] (0.26M). This segmentor serves as a domain-specific feature extractor that captures high-level vascular semantics while remaining computationally efficient and obviating the need for external data.

### C. X-ray Angiogram Analysis

X-ray angiography remains the primary modality for CVDs [3]. While deep learning methods like UNet [34] and Faster R-CNN [35], along with their advanced variants [5]–[7], [36]–[40], have significantly improved segmentation and detection accuracy, they remain constrained by their reliance on fully-supervised learning. Consequently, these methods yield task-specific representations that generalize poorly and fail to exploit vast quantities of unlabeled data [41]. Distinct from these approaches, we propose the first foundation model for X-ray angiogram analysis, utilizing self-supervised learning to extract robust, transferable representations from large-scale unlabeled data.

## III. METHOD

The overall framework of VasoMIM is illustrated in Fig. 3. In the following, we elaborate on VasoMIM step by step. First, we provide a brief explanation about how to extract vascular anatomy via Frangi filter in Sec. III-A. Subsequently,

implementation details of anatomy-guided masking strategy are provided in Sec. III-B. Finally, detailed formulations of anatomical consistency loss are introduced in Sec. III-C.

### A. Frangi Filter as the Anatomical Extractor

We leverage the Hessian-based Frangi filter to extract vascular anatomy in an unsupervised manner. Following the implementation in [42], the procedure consists of three stages.

**Multi-Scale Hessian Analysis.** We compute the vesselness response  $V$  by analyzing the eigenvalues of the Hessian matrix across scales  $\sigma = \{1, 2, 3, 4\}$ . This enhances tubular vascular structures while suppressing background noise.

**Percentile-based Adaptive Thresholding.** To handle contrast variations, we generate a coarse binary mask by thresholding  $V$  at its  $\alpha$ -th percentile ( $\alpha$  is set to 92 by default). This adaptive strategy effectively isolates salient vascular features compared to fixed intensity thresholding.

**Region Growing.** Finally, we apply a region-growing algorithm [43], initialized at the global maximum of  $V$ , to enforce spatial connectivity. This removes isolated artifacts and yields the final binary vascular mask  $B \in \{0, 1\}^{1 \times H \times W}$ .

### B. Anatomy-guided Masking Strategy

Compared to natural images, X-ray angiograms exhibit significantly higher spatial redundancy, as vessels occupy only a minute fraction of the whole images. Generic masking strategies lack anatomical awareness and disproportionately mask background-only patches. Consequently, pre-training is dominated by the reconstruction of non-informative background textures rather than learning vascular representations.

To overcome this bottleneck, we introduce an anatomy-guided masking strategy. Our core insight is that *patches containing dense vascular structures possess higher information density and should be masked with higher probability*. To formalize this, we define a probability distribution  $f$  over the image patches. In our previous work [22], we relied solely on the vascular anatomy  $B$  extracted by Frangi filter [17]. While intuitive, Frangi filter relies on local intensity gradients and can be sensitive to noise or fail to capture faint vessel branches with low contrast, as shown in Fig. 5 (b). To mitigate this, we propose a co-guidance approach. Specifically, we employ a lightweight segmentor, *i.e.*, UNeXt-S [18], trained on pseudo-labels produced by Frangi filter, to generate a semantic probability map  $M \in [0, 1]^{1 \times H \times W}$ . Unlike the hard thresholding of Frangi filter, the segmentor leverages learned inductive biases to provide a smoother, more holistic estimation of vascular regions. We combine this complementary information to form the co-guidance map  $G \in [0, 1]^{1 \times H \times W}$ :

$$G = \eta \cdot B + (1 - \eta) \cdot M \quad (1)$$

where  $\eta$  is set to 0.5 empirically.

During pre-training, the angiogram  $I$  and the corresponding map  $G$  are partitioned into non-overlapping patches  $x \in \mathbb{R}^{N \times (P^2 C)}$  and  $g \in \mathbb{R}^{N \times P^2}$ , respectively, where  $P$  is the patch size and  $N = HW/P^2$  is the sequence length. Let

$g_i \in [0, 1]^{P^2}$  be the  $i$ -th patch of  $g$ . The patch-wise vascular anatomical distribution  $f(g_i)$  is defined as follows:

$$f(g_i) = \frac{\sum_{j=1}^{P^2} g_{ij}}{\sum_{k=1}^N \sum_{j=1}^{P^2} g_{kj}}, \quad i = 1, 2, \dots, N \quad (2)$$

This formulation ensures that patches with higher vessel probabilities are assigned higher sampling weights and is efficiently implemented via `torch.multinomial`.

**Weak-to-Strong Anatomical Guidance.** Masking too many vessel-containing patches in the early training stages may overwhelm the model, impeding convergence. To address this, we implement a weak-to-strong anatomy-guided strategy. As illustrated in Fig. 3, for a specific epoch  $e$ , a fraction  $\beta_e$  of the masked patches are sampled according to  $f(g_i)$ , while the remaining  $1 - \beta_e$  are selected randomly, following standard MAE [10]. The guidance intensity  $\beta_e$  increases linearly:

$$\beta_e = \beta_0 + \frac{e}{E} (\beta_E - \beta_0) \quad (3)$$

where  $E$  is the maximum pre-training epoch, and  $\beta_0, \beta_E \in [0, 1]$  are hyper-parameters. Under this strategy,  $\beta_e \gamma N$  patches are masked based on anatomical guidance, and  $(1 - \beta_e) \gamma N$  patches are masked randomly, where  $\gamma$  is the masking ratio.

### C. Anatomical Consistency Loss

Conventional MIM reconstruction objectives (*e.g.*, MSE) operate in the pixel space, which does not guarantee the consistency of high-level vascular semantics. This is particularly detrimental in X-ray angiograms, where the topology of vascular structures is more critical than exact pixel intensity reconstruction. To bridge this gap, we introduce an anatomical consistency loss that explicitly enforces the preservation of vascular topology in the reconstructed image:

$$\mathcal{L}_{\text{cons.}} = \mathcal{L}(\mathcal{S}(I), \mathcal{S}(I')) \quad (4)$$

where  $I'$  is the reconstructed angiogram.  $\mathcal{L}$  denotes an abstract metric function, and we use cross-entropy by default.  $\mathcal{S}(\cdot)$  represents the semantic extractor. While Frangi filter provides effective masks, its non-differentiable nature precludes its use in an end-to-end pre-training process. Therefore, we utilize the lightweight segmentor introduced in Sec. III-B as a differentiable surrogate.

**Training Objective.** In addition to the anatomical consistency loss, we also use the pixel-level reconstruction loss, *i.e.*, MSE, following conventional MIM approaches [10], [15], [29]. The overall training objective is:

$$\mathcal{L}_{\text{MIM}} = \mathcal{L}_{\text{rec.}} + \mathcal{L}_{\text{cons.}} \quad (5)$$

## IV. RESULTS

### A. Datasets

Table II summarizes the datasets used in the experiments, with downstream tasks illustrated in Fig. 4.

**Pre-training.** XA-170K is collected from four publicly available sources: CADICA [52], SYNTAX [53], XCAD [54], and CoronaryDominance [55]. *i*) CADICA comprises coronary angiography videos from 42 patients, with durations

**TABLE I:** Quantitative comparison on segmentation tasks. We report “mean  $\pm$  std” over five random seeds, excluding Frangi filter. The best results are highlighted in **bold**, and the second-best are underlined.

| Method  | Pre-training Data   | ARCADE-V                |                         | CAXF                    |                         | XCAV                    |                         | ARCADE-S                | ARCADE-VS               | Avg. Rank        |
|---|---------------------|-------------------------|-------------------------|-------------------------|-------------------------|-------------------------|-------------------------|-------------------------|-------------------------|------------------|
|   |                     | DSC (%)                 | clDice (%)              | DSC (%)                 | clDice (%)              | DSC (%)                 | clDice (%)              | DSC (%)                 | DSC (%)                 |                  |
| <i>Traditional</i>                                  |                     |                         |                         |                         |                         |                         |                         |                         |                         |                  |
| Frangi Filter [17] [ <i>MIICCAI'98</i> ]            | —                   | 41.30                   | 40.91                   | 64.01                   | 65.73                   | 58.46                   | 57.15                   | —                       | —                       | —                |
| <i>From Scratch</i>                                 |                     |                         |                         |                         |                         |                         |                         |                         |                         |                  |
| UNet [34] [ <i>MIICCAI'15</i> ]                     | —                   | <u>71.44</u> $\pm$ 0.32 | <u>70.67</u> $\pm$ 0.40 | <u>82.76</u> $\pm$ 0.75 | <u>84.95</u> $\pm$ 0.56 | <u>78.18</u> $\pm$ 0.34 | <u>74.71</u> $\pm$ 0.44 | <u>27.04</u> $\pm$ 3.65 | <u>38.77</u> $\pm$ 0.82 | 22.00 $\pm$ 0.93 |
| TransUNet [38] [ <i>Media'24</i> ]                  | —                   | 75.51 $\pm$ 0.31        | 76.29 $\pm$ 0.37        | 87.90 $\pm$ 0.08        | 90.98 $\pm$ 0.15        | 82.49 $\pm$ 0.98        | 81.00 $\pm$ 0.01        | 46.94 $\pm$ 0.81        | 50.46 $\pm$ 1.29        | 14.00 $\pm$ 3.02 |
| VM-UNet [39] [ <i>ACM TOMM'25</i> ]                 | —                   | 72.62 $\pm$ 2.58        | 72.82 $\pm$ 3.19        | 86.14 $\pm$ 0.21        | 90.11 $\pm$ 0.20        | 81.42 $\pm$ 0.60        | 79.02 $\pm$ 0.72        | 36.92 $\pm$ 1.51        | 44.39 $\pm$ 2.78        | 18.25 $\pm$ 1.83 |
| RWKV-UNet [40] [ <i>arXiv'25</i> ]                  | —                   | 70.56 $\pm$ 0.88        | 72.45 $\pm$ 0.81        | 83.96 $\pm$ 1.02        | 88.02 $\pm$ 1.26        | 81.14 $\pm$ 0.57        | 79.43 $\pm$ 0.74        | 32.79 $\pm$ 4.19        | 50.42 $\pm$ 0.38        | 19.50 $\pm$ 1.77 |
| <i>General SSL</i>                                  |                     |                         |                         |                         |                         |                         |                         |                         |                         |                  |
| MoCo v3 [23] [ <i>ICCV'21</i> ]                     | XA-170K             | 76.08 $\pm$ 0.19        | 76.59 $\pm$ 0.21        | 87.20 $\pm$ 0.36        | 89.27 $\pm$ 0.37        | 83.75 $\pm$ 0.16        | 80.79 $\pm$ 0.21        | 41.71 $\pm$ 0.81        | 49.95 $\pm$ 0.31        | 15.25 $\pm$ 2.60 |
| DINO [24] [ <i>ICCV'21</i> ]                        | XA-170K             | 76.37 $\pm$ 0.17        | 77.04 $\pm$ 0.26        | 87.07 $\pm$ 0.35        | 89.32 $\pm$ 0.41        | 82.28 $\pm$ 0.74        | 79.50 $\pm$ 0.88        | 43.39 $\pm$ 1.11        | 51.08 $\pm$ 0.43        | 15.88 $\pm$ 0.83 |
| iBOT [16] [ <i>ICLR'22</i> ]                        | XA-170K             | 76.58 $\pm$ 0.26        | 77.28 $\pm$ 0.30        | 86.50 $\pm$ 0.40        | 88.89 $\pm$ 0.28        | 80.84 $\pm$ 0.92        | 77.54 $\pm$ 1.20        | 44.50 $\pm$ 0.61        | 54.04 $\pm$ 0.45        | 16.38 $\pm$ 2.77 |
| MAE [10] [ <i>CVPR'22</i> ]                         | XA-170K             | 79.39 $\pm$ 0.15        | 80.74 $\pm$ 0.20        | 89.20 $\pm$ 0.31        | 91.80 $\pm$ 0.36        | 84.84 $\pm$ 1.79        | 82.58 $\pm$ 1.95        | 51.72 $\pm$ 0.54        | 56.69 $\pm$ 0.48        | 4.88 $\pm$ 1.25  |
| SimMIM [25] [ <i>CVPR'22</i> ]                      | XA-170K             | 77.81 $\pm$ 0.22        | 78.84 $\pm$ 0.34        | 88.02 $\pm$ 0.63        | 90.47 $\pm$ 0.66        | 82.77 $\pm$ 0.79        | 80.22 $\pm$ 0.98        | 47.63 $\pm$ 0.69        | 55.17 $\pm$ 0.26        | 12.50 $\pm$ 1.93 |
| AMT [14] [ <i>AAAI'23</i> ]                         | XA-170K             | 78.39 $\pm$ 0.17        | 79.58 $\pm$ 0.16        | 89.15 $\pm$ 0.12        | 91.77 $\pm$ 0.17        | 84.98 $\pm$ 1.11        | 82.58 $\pm$ 0.16        | 48.49 $\pm$ 0.88        | 55.68 $\pm$ 0.39        | 7.38 $\pm$ 2.20  |
| LocalMIM [44] [ <i>CVPR'23</i> ]                    | XA-170K             | 78.79 $\pm$ 0.20        | 80.24 $\pm$ 0.24        | 88.44 $\pm$ 0.70        | 90.87 $\pm$ 0.89        | 83.18 $\pm$ 1.84        | 80.60 $\pm$ 2.10        | 51.20 $\pm$ 0.45        | 57.05 $\pm$ 2.60        | 9.25 $\pm$ 3.62  |
| I-JEPA [45] [ <i>CVPR'23</i> ]                      | XA-170K             | 77.06 $\pm$ 0.17        | 77.80 $\pm$ 0.25        | 88.05 $\pm$ 0.12        | 90.09 $\pm$ 0.15        | 84.30 $\pm$ 0.16        | 81.23 $\pm$ 0.11        | 47.38 $\pm$ 0.86        | 51.87 $\pm$ 0.39        | 12.12 $\pm$ 2.42 |
| HPM [15] [ <i>TPAMI'25</i> ]                        | XA-170K             | 78.84 $\pm$ 0.15        | 80.25 $\pm$ 0.14        | 88.86 $\pm$ 0.24        | 91.48 $\pm$ 0.41        | 85.19 $\pm$ 0.07        | 83.13 $\pm$ 0.13        | 50.06 $\pm$ 0.29        | 56.81 $\pm$ 0.37        | 6.12 $\pm$ 1.81  |
| DINOv3 [46] [ <i>arXiv'25</i> ]                     | LVD-1698M           | 79.36 $\pm$ 0.07        | 80.90 $\pm$ 0.23        | 89.13 $\pm$ 0.26        | <u>92.27</u> $\pm$ 0.44 | 82.76 $\pm$ 2.28        | 80.62 $\pm$ 2.40        | 53.57 $\pm$ 0.81        | 54.36 $\pm$ 0.59        | 7.25 $\pm$ 5.20  |
| <i>Medical SSL</i>                                  |                     |                         |                         |                         |                         |                         |                         |                         |                         |                  |
| Model Genesis <sup>†</sup> [47] [ <i>Media'20</i> ] | XA-170K             | 71.11 $\pm$ 0.21        | 70.75 $\pm$ 0.19        | 83.74 $\pm$ 0.36        | 85.49 $\pm$ 0.41        | 79.74 $\pm$ 0.27        | 76.34 $\pm$ 0.24        | 23.51 $\pm$ 0.66        | 41.26 $\pm$ 0.46        | 21.25 $\pm$ 0.71 |
| LVM-Med [48] [ <i>NeurIPS'23</i> ]                  | Medical-1.3M        | 74.82 $\pm$ 0.20        | 75.57 $\pm$ 0.27        | 85.21 $\pm$ 0.98        | 86.73 $\pm$ 1.23        | 82.47 $\pm$ 0.81        | 80.82 $\pm$ 0.80        | 39.34 $\pm$ 5.10        | 48.09 $\pm$ 0.01        | 17.50 $\pm$ 2.51 |
| DeblurringMIM [29] [ <i>Media'24</i> ]              | XA-170K             | 79.25 $\pm$ 0.13        | 80.77 $\pm$ 0.22        | 89.28 $\pm$ 0.26        | 91.91 $\pm$ 0.35        | 85.38 $\pm$ 0.45        | 83.10 $\pm$ 0.59        | 51.70 $\pm$ 0.81        | 56.66 $\pm$ 0.52        | 4.38 $\pm$ 1.06  |
| RAD-DINO [21] [ <i>Nat. Mach. Intell.'25</i> ]      | LVD-142M & CXR-838K | 78.96 $\pm$ 0.25        | 80.26 $\pm$ 0.40        | 88.76 $\pm$ 0.33        | 91.66 $\pm$ 0.59        | 84.88 $\pm$ 0.29        | 83.29 $\pm$ 0.47        | 51.55 $\pm$ 0.63        | 54.81 $\pm$ 0.15        | 6.62 $\pm$ 2.26  |
| Frepa [49] [ <i>TM'25</i> ]                         | XA-170K             | 70.97 $\pm$ 0.29        | 70.07 $\pm$ 0.54        | 82.88 $\pm$ 0.12        | 84.79 $\pm$ 1.24        | 78.28 $\pm$ 0.43        | 74.67 $\pm$ 0.60        | 27.97 $\pm$ 3.59        | 38.12 $\pm$ 1.16        | 22.38 $\pm$ 0.74 |
| CheXWorld [50] [ <i>CVPR'25</i> ]                   | XA-170K             | 78.18 $\pm$ 0.24        | 79.40 $\pm$ 0.35        | 88.52 $\pm$ 0.22        | 90.87 $\pm$ 0.35        | 83.81 $\pm$ 0.79        | 80.95 $\pm$ 0.91        | 49.69 $\pm$ 0.65        | 55.81 $\pm$ 0.33        | 9.88 $\pm$ 1.46  |
| MedDINOv3 [51] [ <i>arXiv'25</i> ]                  | LVD-1698M & CT-3M   | 78.38 $\pm$ 0.20        | 79.53 $\pm$ 0.29        | 88.43 $\pm$ 0.28        | 90.96 $\pm$ 0.38        | 83.62 $\pm$ 2.43        | 81.24 $\pm$ 2.86        | 49.97 $\pm$ 0.52        | 54.98 $\pm$ 0.38        | 9.88 $\pm$ 0.99  |
| VasoMIM-v1 [22] [ <i>AAAI'26</i> ]                  | XA-170K             | 79.90 $\pm$ 0.16        | 81.57 $\pm$ 0.28        | 89.36 $\pm$ 0.20        | 92.19 $\pm$ 0.36        | 85.80 $\pm$ 0.27        | 83.75 $\pm$ 0.37        | 54.52 $\pm$ 0.53        | 58.03 $\pm$ 0.27        | 2.12 $\pm$ 0.35  |
| VasoMIM [ <i>Ours</i> ]                             | XA-170K             | <b>80.25</b> $\pm$ 0.12 | <b>82.06</b> $\pm$ 0.18 | <b>89.68</b> $\pm$ 0.08 | <b>92.57</b> $\pm$ 0.12 | <b>86.09</b> $\pm$ 0.09 | <b>84.12</b> $\pm$ 0.17 | <b>55.62</b> $\pm$ 0.63 | <b>58.87</b> $\pm$ 0.15 | 1.00 $\pm$ 0.00  |
| $\Delta$ vs. UNet                                   | —                   | —                       | ↑ 8.81                  | ↑ 11.39                 | ↑ 6.92                  | ↑ 7.62                  | ↑ 7.91                  | ↑ 9.41                  | ↑ 28.58                 | ↑ 20.10          |

†: We implement the 2D version of Model Genesis based on the official codebase.

**TABLE II:** Statistics of XA-170K and downstream datasets.

| Usage        | Dataset                | #train  | #test |
|--------------|------------------------|---------|-------|
| Pre-training | CADICA [52]            | 6,594   | —     |
|              | SYNTAX [53]            | 2,943   | —     |
|              | XCAD [54]              | 1,621   | —     |
|              | CoronaryDominance [55] | 160,320 | —     |
| Segmentation | Total                  | 171,478 | —     |
|              | ARCADE-V [56]          | 1,000   | 300   |
|              | ARCADE-VS [56]         | 1,000   | 300   |
|              | CAXF [36]              | 337     | 201   |
| Detection    | XCAV [42]              | 175     | 46    |
|              | Stenosis [57]          | 7,492   | 833   |

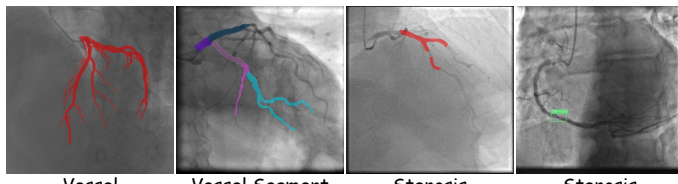


Fig. 4: Overview of downstream tasks.

ranging from 1 to 151 frames. From these, we select 6,594 high-quality frames. *ii) SYNTAX* contains 2,943 X-ray angiograms derived from 231 patients. *iii) XCAD* provides a set of 1,747 angiograms, from which 1,621 images are utilized. *iv) CoronaryDominance* consists of videos from 1,574 patients. We extract informative frames from each video sequence, yielding a total of 160,320 images.

**Segmentation.** We evaluate VasoMIM across three distinct segmentation tasks: vessel segmentation (ARCADE-VS, CAXF, and XCAV), vessel segment segmentation (ARCADE-

VS), and stenosis segmentation (ARCADE-S). *i) ARCADE* is divided into two subsets: one dedicated to vessel (V) and vessel segment (VS) segmentation, and another for stenosis (S) segmentation. Each subset contains 1,300 images, partitioned into training (1,000) and testing (300) sets. *ii) CAXF* consists of 538 images derived from 36 angiography videos. Following [5], [36], 337 frames from 24 videos are utilized for training, while the remaining 201 images from 12 videos are reserved for testing. *iii) XCAV* comprises 111 videos from 59 patients. Frames with pixel-level vessel annotations are extracted and split by patient ID, resulting in 175 training frames (47 patients) and 46 test frames (12 patients).

**Detection.** For this task, we utilize **Stenosis**, which contains angiography videos from 100 patients totaling 8,325 frames. The dataset is split into a training set of 7,492 frames (90 patients) and a testing set of 833 frames (10 patients).

### B. Implementation Details

**Pre-training.** Our pre-training configuration largely follows the standard MAE protocol [10]. We utilize ViT-B/16 [58] as the default backbone unless stated otherwise. VasoMIM is pre-trained for 800 epochs, which requires approximately ten hours on 8×NVIDIA H20 GPUs.

**Segmentation.** We adopt UNet [34] as the segmentation framework, performing end-to-end fine-tuning at a resolution of  $224 \times 224$ . To enhance feature aggregation, we upgrade the standard UNet decoder used in our previous work [22] by incorporating a SimpleFPN [59] adaptor, following the implementation in CheXWorld [50]. Optimization is performed using AdamW with a cosine-annealing schedule, where  $T_{\max} = \text{Epoch}_{\max}$ . All downstream segmentation experiments are conducted on a single NVIDIA H20 GPU. The specific hyper-parameters for each dataset are detailed below:

**TABLE III:** Quantitative results for the stenosis detection task. We report “mean  $\pm$  std” over five random seeds. The best and second-best results are highlighted in **bold** and underlined, respectively.

| Method   | Pre-training Data  | mAP50 (%)                        | mAP75 (%)                        | mAP (%)                          | Avg. Rank                       |
|--|--------------------|----------------------------------|----------------------------------|----------------------------------|---------------------------------|
| <i>From Scratch</i>                                |                    |                                  |                                  |                                  |                                 |
| Faster R-CNN [35] [ <i>FPN</i> ’16]                | —                  | 88.37 $\pm$ 0.90                 | 19.01 $\pm$ 1.77                 | 36.63 $\pm$ 0.63                 | 20.33 $\pm$ 0.58                |
| DETR [60] [ <i>ViT</i> ’20]                        | —                  | 89.30 $\pm$ 0.79                 | 19.35 $\pm$ 0.00                 | 36.51 $\pm$ 0.57                 | 19.00 $\pm$ 2.65                |
| <i>General SSL</i>                                 |                    |                                  |                                  |                                  |                                 |
| MoCo v3 [23] [ <i>ICCV</i> ’21]                    | XA-170K            | 91.54 $\pm$ 1.04                 | 21.74 $\pm$ 0.67                 | 38.74 $\pm$ 0.32                 | 14.00 $\pm$ 1.00                |
| DINO [24] [ <i>ICCV</i> ’21]                       | XA-170K            | 88.83 $\pm$ 0.46                 | 21.12 $\pm$ 0.78                 | 37.65 $\pm$ 0.41                 | 17.00 $\pm$ 1.00                |
| iBOT [16] [ <i>ICLR</i> ’22]                       | XA-170K            | 92.16 $\pm$ 0.85                 | 23.94 $\pm$ 0.68                 | 39.76 $\pm$ 0.30                 | 9.67 $\pm$ 2.00                 |
| MAE [10] [ <i>CVPR</i> ’22]                        | XA-170K            | 92.30 $\pm$ 0.42                 | 24.28 $\pm$ 0.66                 | 39.69 $\pm$ 0.48                 | 9.67 $\pm$ 2.31                 |
| SimMIM [25] [ <i>CVPR</i> ’22]                     | XA-170K            | 89.84 $\pm$ 0.72                 | 22.30 $\pm$ 0.27                 | 38.29 $\pm$ 0.38                 | 15.00 $\pm$ 1.00                |
| AMT [14] [ <i>AAAI</i> ’23]                        | XA-170K            | 93.35 $\pm$ 1.20                 | 24.35 $\pm$ 0.08                 | 40.23 $\pm$ 0.59                 | 7.00 $\pm$ 1.00                 |
| LocalMIM [44] [ <i>CVPR</i> ’23]                   | XA-170K            | 93.59 $\pm$ 0.53                 | 24.76 $\pm$ 0.47                 | 40.24 $\pm$ 0.61                 | 5.00 $\pm$ 1.73                 |
| I-JEPA [45] [ <i>CVPR</i> ’23]                     | XA-170K            | 90.47 $\pm$ 0.89                 | 22.51 $\pm$ 1.36                 | 38.63 $\pm$ 0.75                 | 14.00 $\pm$ 1.00                |
| HPM [15] [ <i>TPAMI</i> ’25]                       | XA-170K            | 92.47 $\pm$ 0.36                 | 24.65 $\pm$ 1.12                 | 40.53 $\pm$ 0.35                 | 6.67 $\pm$ 2.89                 |
| DINOv3 [46] [ <i>arXiv</i> ’25]                    | LVD-1698M          | 93.89 $\pm$ 0.81                 | 23.60 $\pm$ 1.87                 | 40.90 $\pm$ 0.39                 | 5.33 $\pm$ 4.04                 |
| <i>Medical SSL</i>                                 |                    |                                  |                                  |                                  |                                 |
| Model Genesis <sup>†</sup> [47] [ <i>MedI</i> ’20] | XA-170K            | 87.81 $\pm$ 1.06                 | 19.96 $\pm$ 0.81                 | 36.89 $\pm$ 0.46                 | 19.33 $\pm$ 1.53                |
| LVM-Med [48] [ <i>MedI</i> ’20]                    | Medical-1.3M       | 93.64 $\pm$ 0.88                 | 23.14 $\pm$ 0.89                 | 39.75 $\pm$ 0.40                 | 9.00 $\pm$ 3.61                 |
| DeblurringMIM [29] [ <i>MedI</i> ’24]              | XA-170K            | 88.99 $\pm$ 0.96                 | 24.73 $\pm$ 1.60                 | 39.26 $\pm$ 0.65                 | 11.33 $\pm$ 6.66                |
| RAD-DINO [21] [ <i>Nat. Mach. Inell.</i> ’25]      | LVD-142M & CXR-83K | 93.56 $\pm$ 0.29                 | 23.92 $\pm$ 1.33                 | 40.64 $\pm$ 0.63                 | 6.67 $\pm$ 2.52                 |
| Frepa [49] [ <i>TPAMI</i> ’25]                     | XA-170K            | 88.61 $\pm$ 0.82                 | 19.82 $\pm$ 0.88                 | 37.22 $\pm$ 0.27                 | 18.67 $\pm$ 0.58                |
| CheXWorld [50] [ <i>CVPR</i> ’25]                  | XA-170K            | 92.89 $\pm$ 1.02                 | 23.48 $\pm$ 1.11                 | 40.16 $\pm$ 0.98                 | 9.33 $\pm$ 1.00                 |
| MedDINOv3 [51] [ <i>arXiv</i> ’25]                 | LVD-1698M & CT-3M  | 93.79 $\pm$ 0.47                 | 20.96 $\pm$ 1.72                 | 39.69 $\pm$ 0.64                 | 10.67 $\pm$ 6.51                |
| VasoMIM-v1 [22] [ <i>AAAI</i> ’26]                 | XA-170K            | <b>94.25<math>\pm</math>0.72</b> | <u>25.01<math>\pm</math>1.21</u> | <b>40.91<math>\pm</math>0.63</b> | <u>2.00<math>\pm</math>0.00</u> |
| VasoMIM [ <i>Our</i> ]                             | XA-170K            | <b>94.91<math>\pm</math>0.28</b> | <u>25.72<math>\pm</math>1.57</u> | <b>41.07<math>\pm</math>0.35</b> | <b>1.00<math>\pm</math>0.00</b> |
| Δ vs. Faster R-CNN                                 | —                  | <b>↑ 6.54</b>                    | <u>↑ 6.71</u>                    | <b>↑ 4.44</b>                    | —                               |

†: We implement the 2D version of Model Genesis based on the official codebase.

- ARCADE-V:  $lr_{base} = 2e^{-4}$ , Epoch<sub>max</sub> = 100
- CAXF:  $lr_{base} = 4e^{-4}$ , Epoch<sub>max</sub> = 200
- XCAV:  $lr_{base} = 6e^{-4}$ , Epoch<sub>max</sub> = 200
- ARCADE-S:  $lr_{base} = 8e^{-5}$ , Epoch<sub>max</sub> = 100
- ARCADE-VS:  $lr_{base} = 1e^{-4}$ , Epoch<sub>max</sub> = 100

**Detection.** For stenosis detection, we employ Faster R-CNN [35] with FPN [61]. The model is fine-tuned end-to-end for 100 epochs at a resolution of  $512 \times 512$  on a single NVIDIA H20 GPU. We adhere to the standard ViTDet [59] configurations as implemented in Detectron<sup>1</sup>.

**Evaluation Metrics.** For all segmentation tasks, we report the dice similarity coefficient (DSC). Additionally, given the thin and curvilinear characteristic of vascular structures, we report centerlineDice (clDice) [62] exclusively for vessel segmentation tasks to better quantify topological correctness. For detection tasks, we report the mean average precision (mAP), including mAP50 and mAP75, as well as the mAP averaged across IoU thresholds from 0.50 to 0.95.

### C. Main Results

All baselines are implemented using their official codebases. To ensure a rigorous comparison, each model is fine-tuned across five random seeds under the same configurations. We report all metrics as “mean  $\pm$  std”.

**Segmentation.** Several key findings can be observed from Table I: *i) Pre-training unlocks the potential of segmentors.* By pre-training on large-scale unlabeled data, UNet [34] significantly outperforms advanced segmentors with complex architectures trained from scratch [38]–[40]. *ii) VasoMIM establishes a new state-of-the-art.* Our method consistently surpasses all SSL alternatives by a clear margin. Notably, even DINOv3 [46], the leading vision foundation model pre-trained on 1.6 billion images, lags behind VasoMIM. This underscores the critical necessity of domain-specific pre-training. *iii) Robustness on challenging tasks.* The advantage of VasoMIM is even more pronounced on complex tasks, such as stenosis

**TABLE IV:** Ablation study of the anatomy-guided masking strategy and the anatomical consistency loss.

| Guidance | $\mathcal{L}_{cons.}$ | ARCADE-V                |                         | XCAV                    |                         |
|----------|-----------------------|-------------------------|-------------------------|-------------------------|-------------------------|
|          |                       | DSC (%)                 | clDice (%)              | DSC (%)                 | clDice (%)              |
| —        | —                     | 79.31 $\pm$ 0.16        | 81.05 $\pm$ 0.25        | 84.52 $\pm$ 2.12        | 82.25 $\pm$ 2.32        |
| —        | ✓                     | 79.85 $\pm$ 0.14        | <b>81.59</b> $\pm$ 0.16 | 85.79 $\pm$ 0.52        | 83.66 $\pm$ 0.77        |
| ✓        | —                     | <b>79.87</b> $\pm$ 0.09 | 81.41 $\pm$ 0.11        | <b>85.92</b> $\pm$ 0.04 | <b>83.78</b> $\pm$ 0.15 |
| ✓        | ✓                     | <b>80.25</b> $\pm$ 0.12 | <b>82.06</b> $\pm$ 0.18 | <b>86.09</b> $\pm$ 0.09 | <b>84.12</b> $\pm$ 0.17 |

segmentation (ARCADE-S) and vessel segment segmentation (ARCADE-VS). This widening gap highlights VasoMIM’s superior generalizability and its ability to capture fine-grained topological details where baselines falter.

**Detection.** Table III presents the quantitative results on the stenosis detection task. VasoMIM delivers substantial improvements over the supervised baseline. Among the SSL baselines, LocalMIM [44] emerges as the strongest competitor. Nevertheless, VasoMIM consistently surpasses this method, achieving further gains of +1.32% mAP50, +0.96% mAP75, and +0.83% mAP. These results underscore the superiority of our domain-specific pre-training framework in learning robust representations for localizing lesion features.

**Overall Improvements over VasoMIM-v1 [22].** Notably, VasoMIM consistently surpasses its conference version, VasoMIM-v1 [22], across all segmentation and detection metrics ( $p$  – value =  $1.18 \times 10^{-4}$ , paired t-test).

### D. Ablation Study

Ablation studies are conducted on ARCADE-V and XCAV. Default settings are highlighted in blue. Table IV reports the quantitative results of sequentially integrating each proposed component into the vanilla baseline, *i.e.*, MAE ( $\gamma = 0.5$ ).

**Efficacy of Anatomy-Guided Masking Strategy.** Integrating the proposed anatomy-guided masking strategy yields an obvious performance boost. Here, we provide detailed analysis to elucidate the mechanism behind these improvements. As illustrated in Fig. 5 (a), our strategy gradually increases the focus on vessel-containing patches, whereas the baseline masks a relatively small and constant proportion. We further visualize the patch-wise masking ratio in Fig. 5 (b). While the single-guidance strategy [22] favors vessel-containing patches, it misses vital vessel branches due to the limitations of Frangi filter. In contrast, our proposed co-guidance strategy, which integrates the strong inductive bias of the segmentor, captures vascular anatomy with higher fidelity, ensuring the model focuses on the most discriminative regions.

**Significance of Anatomical Consistency Loss.** The anatomical consistency loss enhances performance of the baseline by +0.56% and +1.40% DSC on ARCADE-V and XCAV, respectively. To further verify the superiority of  $\mathcal{L}_{cons.}$ , we compare it against alternative reconstruction objectives in Table V. Our method offers two distinct advantages: *i) Superior Downstream Performance.* It consistently outperforms feature distillation and perceptual loss methods. *ii) Negligible Computational Overhead.* Unlike other objectives

<sup>1</sup><https://github.com/facebookresearch/detectron2>

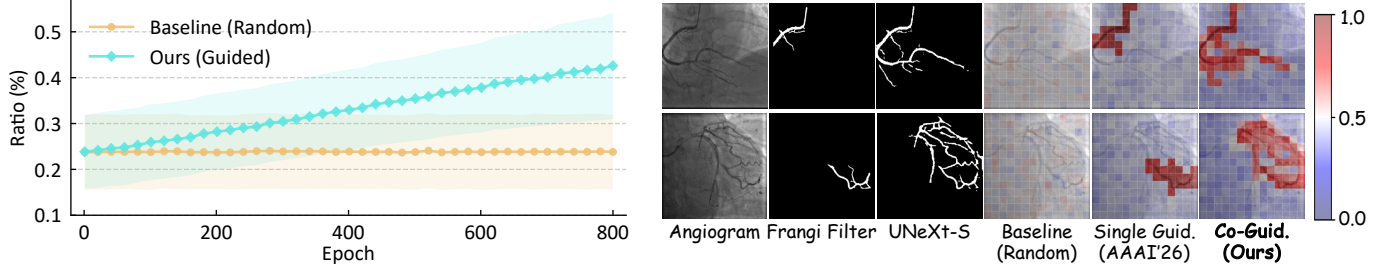


**Fig. 5:** Qualitative analysis of the anatomy-guided masking strategy. **Left:** The proportion of vessel-containing patches among all masked patches across training epochs. **Right:** Visual comparison. We highlight failure cases of Frangi filter where UNeXt-S, leveraging strong inductive bias, extracts vascular anatomy more accurately to provide precise guidance. The heatmaps display the patch-wise masking ratio, *i.e.*,  $\frac{1}{E} \sum_{j=1}^E \mathbb{I}(\text{Patch } x_i \text{ is masked in epoch } j)$ .

**TABLE V:** Comparison with alternative reconstruction objectives. GFLOPs are calculated on an NVIDIA H20 GPU using a single  $224 \times 224$  masked RGB image. DSC is reported in this table.

| Loss                               | Params. (M)               | FLOPs (G)                          | ARCADE-V                           | XCAV                               |
|------------------------------------|---------------------------|------------------------------------|------------------------------------|------------------------------------|
| <i>Baseline</i>                    | —                         | 111.91                             | 19.01                              | $79.87 \pm 0.09$                   |
| <i>Feature Distillation</i>        |                           |                                    |                                    |                                    |
| DINO [24] [ <i>ICCV'21</i> ]       | 197.95                    | 52.90                              | $79.81 \pm 0.12$                   | $85.03 \pm 2.27$                   |
| $\textcolor{red}{+86.04}$          | $\textcolor{red}{+33.89}$ | $\textcolor{red}{\downarrow 0.06}$ | $\textcolor{red}{\downarrow 0.89}$ | $\textcolor{red}{\downarrow 0.89}$ |
| CLIP [63] [ <i>ICML'21</i> ]       | 169.43                    | 41.66                              | $79.79 \pm 0.13$                   | $85.29 \pm 1.47$                   |
| $\textcolor{red}{+57.52}$          | $\textcolor{red}{+22.65}$ | $\textcolor{red}{\downarrow 0.08}$ | $\textcolor{red}{\downarrow 0.63}$ | $\textcolor{red}{\downarrow 0.63}$ |
| DINOv3 [46] [ <i>arXiv'25</i> ]    | 176.69                    | 45.04                              | $80.03 \pm 0.11$                   | $86.04 \pm 0.09$                   |
| $\textcolor{red}{+64.78}$          | $\textcolor{red}{+26.03}$ | $\textcolor{green}{\uparrow 0.16}$ | $\textcolor{green}{\uparrow 0.12}$ | $\textcolor{green}{\uparrow 0.12}$ |
| EMA                                | 197.95                    | 52.90                              | $80.05 \pm 0.12$                   | $86.00 \pm 0.09$                   |
| $\textcolor{red}{+86.04}$          | $\textcolor{red}{+33.89}$ | $\textcolor{green}{\uparrow 0.18}$ | $\textcolor{green}{\uparrow 0.08}$ | $\textcolor{green}{\uparrow 0.08}$ |
| <i>Perceptual Loss</i>             |                           |                                    |                                    |                                    |
| LPIPS [64] [ <i>CVPR'18</i> ]      | 126.63                    | 80.45                              | $79.18 \pm 0.14$                   | $86.00 \pm 0.08$                   |
| $\textcolor{red}{+14.72}$          | $\textcolor{red}{+61.44}$ | $\textcolor{red}{\downarrow 0.69}$ | $\textcolor{green}{\uparrow 0.08}$ | $\textcolor{green}{\uparrow 0.08}$ |
| Contextual [65] [ <i>ECCV'18</i> ] | 131.93                    | 97.05                              | $79.90 \pm 0.10$                   | $85.63 \pm 0.91$                   |
| $\textcolor{red}{+20.02}$          | $\textcolor{red}{+78.04}$ | $\textcolor{green}{\uparrow 0.03}$ | $\textcolor{red}{\downarrow 0.29}$ | $\textcolor{red}{\downarrow 0.29}$ |
| $\mathcal{L}_{\text{cons.}}$       | 111.91                    | 19.17                              | $80.25 \pm 0.12$                   | $86.09 \pm 0.09$                   |
|                                    | 0.00                      | $\textcolor{red}{+0.16}$           | $\textcolor{green}{\uparrow 0.38}$ | $\textcolor{green}{\uparrow 0.17}$ |

which require substantial FLOPs,  $\mathcal{L}_{\text{cons.}}$  incurs minimal cost ( $+0.16$  GFLOPs). Furthermore, we analyze the clustering properties of the learned representations. We first split patches into vessel-containing and background-only groups, then use t-SNE [66] to project representations into a low-dimensional space. As reported in Table VI, the model trained with  $\mathcal{L}_{\text{cons.}}$  achieves the best clustering performance, indicating that it learns more discriminative vascular representations.

## V. IN-DEPTH ANALYSIS

In this section, we present a comprehensive analysis of VasoMIM. Unless otherwise specified, all experiments are conducted on ARCADE-V and XCAV. For clarity, the default configurations of VasoMIM are highlighted in blue.

### A. Masking Strategies

**Impact of Guidance Components.** We validate the necessity of the co-guidance approach by adjusting  $\eta$  to isolate the individual contributions of Frangi filter ( $\eta = 1$ ) and the probability map ( $\eta = 0$ ). As shown in Table VII, while both single-guidance approaches improve upon the random baseline, our approach achieves superior performance, confirming the synergistic value of co-guidance. Furthermore, we investigate the

**TABLE VI:** Comparison of clustering metrics on XCAV *training set*. SS: Silhouette Score. CHI ( $\times 10^5$ ): Calinski-Harabasz Index. DBI: Davies-Bouldin Index.

| Loss                               | SS $\uparrow$ | CHI $\uparrow$ | DBI $\downarrow$ |
|------------------------------------|---------------|----------------|------------------|
| <i>Baseline</i>                    | —             | 0.27           | 1.39             |
| <i>Feature Distillation</i>        |               |                |                  |
| DINO [24] [ <i>ICCV'21</i> ]       | 0.03          | 0.06           | 6.42             |
| CLIP [63] [ <i>ICML'21</i> ]       | 0.08          | 0.18           | 3.71             |
| DINOv3 [46] [ <i>arXiv'25</i> ]    | 0.29          | 1.65           | 1.24             |
| EMA                                | 0.27          | 1.53           | 1.33             |
| <i>Perceptual Loss</i>             |               |                |                  |
| LPIPS [64] [ <i>CVPR'18</i> ]      | 0.09          | 0.18           | 3.69             |
| Contextual [65] [ <i>ECCV'18</i> ] | 0.26          | 1.27           | 1.42             |
| $\mathcal{L}_{\text{cons.}}$       | <b>0.32</b>   | <b>2.05</b>    | <b>1.13</b>      |

**TABLE VII:** Impact of different guidance component and sampling strategies. DSC is reported in this table.

| Guidance      | Sampling | ARCADE-V         | XCAV                               |
|---------------|----------|------------------|------------------------------------|
| —             | Random   | $79.85 \pm 0.14$ | $85.79 \pm 0.52$                   |
| Frangi Filter |          | $79.90 \pm 0.16$ | $\textcolor{green}{\uparrow 0.05}$ |
| Prob. Map     | $f(g_i)$ | $79.98 \pm 0.13$ | $\textcolor{green}{\uparrow 0.13}$ |
| Co-Guidance   |          | $80.25 \pm 0.12$ | $\textcolor{green}{\uparrow 0.40}$ |
| Co-Guidance   | Random   | $79.99 \pm 0.14$ | $\textcolor{green}{\uparrow 0.14}$ |

criticality of the patch-wise vascular anatomical distribution  $f(g_i)$ . Replacing it with a uniform random sampling over vascular patches leads to suboptimal results. This finding suggests that prioritizing patches with higher vascular density, rather than treating all vessel-containing patches equally, is essential for efficient representation learning.

**Weak-to-Strong Design.** We further investigate the optimal scheduling of anatomical guidance by varying  $\beta_0$  and  $\beta_E$ . From Table VIII, we observe that maintaining relatively strong guidance degrades performance. This result is intuitive since aggressive masking of all vessel-containing patches eliminates the semantic context necessary for reconstruction, forcing the model to solve an ill-posed problem based solely on background noise. Furthermore, we evaluate a reversed strong-to-weak approach. This approach underperforms even the fully random baseline, underscoring the critical importance of the proposed weak-to-strong design, which progressively increases task difficulty to ensure stable representation learning.

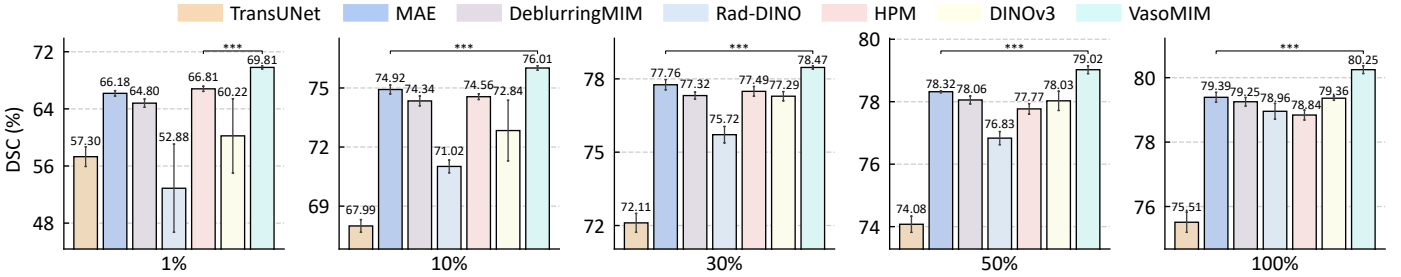


Fig. 6: Label-efficient fine-tuning on ARCADE-V. \*\*\*:  $p < 0.001$  (paired t-test).

TABLE VIII: Evaluation of different masking strategies. DSC is reported in this table.

| Case   | Manner         | $\beta_0$ | $\beta_E$ | ARCADE-V                   | XCAV                       |
|--------|----------------|-----------|-----------|----------------------------|----------------------------|
| Guided | Weak-to-Strong | —         | 0         | $79.85 \pm 0.14$           | $85.79 \pm 0.52$           |
|        |                |           | 0.5       | $80.25 \pm 0.12$<br>↑ 0.40 | $86.09 \pm 0.09$<br>↑ 0.30 |
|        |                | 0         | 0.75      | $79.91 \pm 0.13$<br>↑ 0.06 | $85.99 \pm 0.07$<br>↑ 0.20 |
|        |                | 0         | 1         | $79.96 \pm 0.06$<br>↑ 0.11 | $85.94 \pm 0.13$<br>↑ 0.15 |
|        |                | 1         | 1         | $78.04 \pm 0.12$<br>↓ 1.81 | $83.89 \pm 1.53$<br>↓ 1.90 |
|        | Strong-to-Weak | 0.5       | 0         | $79.79 \pm 0.07$<br>↓ 0.06 | $85.63 \pm 0.34$<br>↓ 0.16 |

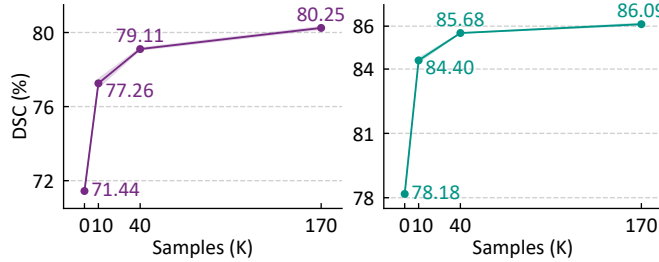


Fig. 7: Data scaling analysis. Left: ARCADE-V. Right: XCAV.

### B. Scaling Law

We investigate the scaling capability of VasoMIM regarding both data scale and model capacity. *i) Data Scaling.* We scale the pre-training dataset from 10K to 170K and evaluate downstream performance in Fig. 7. The performance gradually increases with more data. However, we find that the performance gain from 40K to 170K is less pronounced than the initial leap from 10K to 40K. This phenomenon mirrors findings in recent medical SSL studies, such as VoCo [19]. *ii) Model Scaling.* We further scale the backbone from ViT-B (86M) to ViT-L (307M) and ViT-H (632M). As illustrated in Fig. 8, while increasing model capacity consistently yields higher DSC, the improvements are marginal relative to the substantial increase in computational cost.

We hypothesize three primary factors contributing to the above results: *i) Architectural Bottlenecks.* In this study, we mainly focus on developing a domain-specific pre-training framework instead of designing novel architectures. The segmentor, *i.e.*, UNet [34], may lack scalability. *ii) Data Quality.* XA-170K inevitably contains variable image quality and ar-

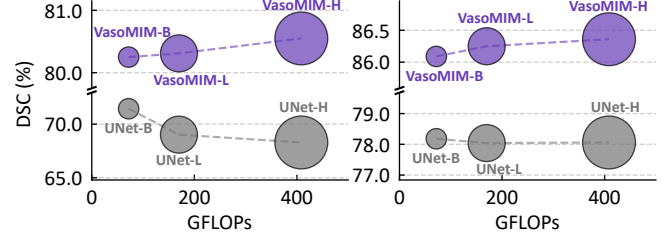


Fig. 8: Scalability analysis of VasoMIM. Left: ARCADE-V. Right: XCAV.

TABLE IX: Impact of pre-training dataset. DSC is reported in this table.

| Method                        | Pre-training Data | ARCADE-V         | XCAV             |
|-------------------------------|-------------------|------------------|------------------|
| MAE [10] [CVPR'22]            | ImageNet-1K       | $78.10 \pm 0.21$ | $83.69 \pm 1.48$ |
|                               | XA-170K           | $79.39 \pm 0.15$ | $84.84 \pm 1.79$ |
|                               | $\Delta$          | ↑ 1.29           | ↑ 1.15           |
| LocalMIM [44] [CVPR'23]       | ImageNet-1K       | $77.55 \pm 0.66$ | $83.00 \pm 0.61$ |
|                               | XA-170K           | $78.79 \pm 0.20$ | $83.18 \pm 1.84$ |
|                               | $\Delta$          | ↑ 1.24           | ↑ 0.18           |
| DeblurringMIM [29] [MedIA'24] | US-Esaote-280K    | $77.80 \pm 0.24$ | $84.46 \pm 0.10$ |
|                               | XA-170K           | $79.25 \pm 0.13$ | $85.38 \pm 0.45$ |
|                               | $\Delta$          | ↑ 1.45           | ↑ 0.92           |
| CheXWorld [50] [CVPR'25]      | X-rays-500K       | $77.12 \pm 0.37$ | $82.12 \pm 1.10$ |
|                               | XA-170K           | $78.18 \pm 0.24$ | $83.81 \pm 0.79$ |
|                               | $\Delta$          | ↑ 1.06           | ↑ 1.69           |
| HPM [15] [TPAMI'25]           | ImageNet-1K       | $78.45 \pm 0.06$ | $84.82 \pm 0.16$ |
|                               | XA-170K           | $78.84 \pm 0.15$ | $85.19 \pm 0.07$ |
|                               | $\Delta$          | ↑ 0.39           | ↑ 0.37           |

titifacts, which may degrade representation learning. *iii) Convergence.* Given that VasoMIM already delivers substantial improvements over the baseline, the performance may be approaching the theoretical upper bound.

### C. Label Efficiency

We compare VasoMIM against five leading SSL baselines and the best fully-supervised method under data-scarce scenarios. As illustrated in Fig. 6, VasoMIM consistently outperforms all competing methods across every data scale. It is worth noting that VasoMIM, using the UNet [34] backbone and fine-tuned on only 10% of the labeled data, achieves 76.01% DSC. This performance surpasses the best fully-supervised baseline, TransUNet [38], trained on 100% of the labeled data by +0.50%. These findings highlight that VasoMIM reduces the annotation requirement by an order of magnitude, underscoring the value of large-scale pre-training.

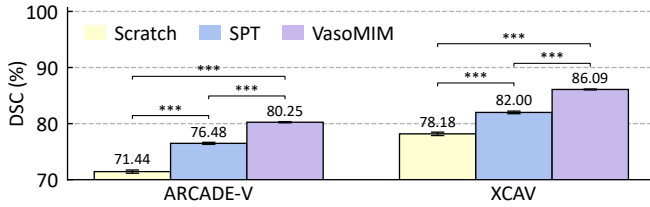


Fig. 9: Segmentor-based Pre-training (SPT) vs. MIM.

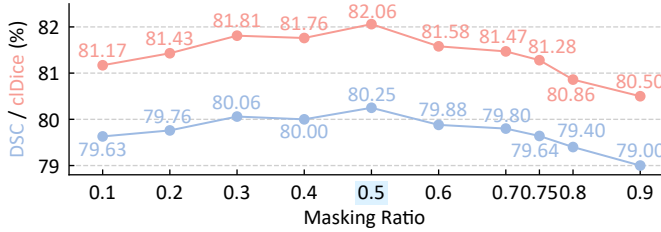


Fig. 10: Hyper-parameter sensitivity of the masking ratio  $\gamma$  on ARCADE-V. All results are averaged under five random seeds.

#### D. Effectiveness of Domain-specific Pre-training Dataset

We select five representative SSL methods to validate the contribution of the introduced XA-170K. Specifically, three generic vision baseline methods [10], [15], [44] are pre-trained on ImageNet-1K, and two medical-domain methods (DeblurringMIM [29] and CheXWorld [50]) are pre-trained on ultrasound and chest X-ray data, respectively. We utilize their officially released checkpoints for fine-tuning. As demonstrated in Table IX, pre-training on XA-170K consistently yields superior performance.

#### E. Segmentor-based Pre-training vs. MIM

To verify that the performance gains stem from our method rather than merely the exposure to additional vascular anatomical data, we compare VasoMIM against a segmentor-based pre-training (SPT) baseline. Specifically, UNet is pre-trained in a fully supervised manner using pseudo-labels generated by Frangi filter on XA-170K. As illustrated in Fig. 9, while SPT provides significant improvement over training from scratch, it consistently lags behind VasoMIM. This gap indicates that SPT is likely limited by the noise inherent in the pseudo-labels generated by Frangi filter.

#### F. Hyper-parameter Analysis

**Masking Ratio.** Fig. 10 illustrates the impact of varying the masking ratio  $\gamma$  on ARCADE-V. We observe that a moderate masking ratio (*i.e.*,  $\gamma = 0.50$ ) yields optimal results. This finding diverges from established practices in the general vision domain, where higher ratios (*e.g.*,  $\gamma = 0.75$  in MAE [10]) are typically preferred. We attribute this discrepancy to the intrinsic characteristics of X-ray angiograms. Unlike natural images, which exhibit high spatial redundancy, angiograms are characterized by sparse vascular structures. Consequently, employing excessively high masking ratios tends to obscure the sparse anatomical cues essential for reconstruction. This

TABLE X: Robustness analysis of VasoMIM under varying qualities of vascular anatomy.

| $\alpha$ | Method  | ARCADE-V         |                  | XCAV             |                  |
|----------|---------|------------------|------------------|------------------|------------------|
|          |         | DSC (%)          | clDice (%)       | DSC (%)          | clDice (%)       |
| 50       | Frangi  | 12.06            | 8.20             | 32.16            | 22.58            |
|          | VasoMIM | $79.71 \pm 0.12$ | $81.26 \pm 0.21$ | $86.02 \pm 0.08$ | $84.05 \pm 0.12$ |
| 80       | Frangi  | 27.06            | 22.34            | 66.70            | 62.51            |
|          | VasoMIM | $79.67 \pm 0.18$ | $81.31 \pm 0.22$ | $86.03 \pm 0.06$ | $84.03 \pm 0.18$ |
| 92       | Frangi  | 41.30            | 40.91            | 58.46            | 57.15            |
|          | VasoMIM | $80.25 \pm 0.12$ | $82.06 \pm 0.18$ | $86.09 \pm 0.09$ | $84.12 \pm 0.17$ |

forces the model to focus on reconstructing non-informative background noise rather than learning vascular representations.

**Quality of Vascular Anatomy.** We investigate the robustness of VasoMIM to the quality of the extracted vascular anatomy. As detailed in Table X, the segmentation performance of Frangi filter fluctuates drastically depending on  $\alpha$ . This indicates significant variation in the quality of the vascular anatomy. Remarkably, the downstream performance of VasoMIM remains highly stable.

## VI. CONCLUSION

In this paper, we present **VasoMIM**, a **Vascular anatomy-aware Masked Image Modeling** framework for large-scale X-ray angiogram pre-training. By explicitly integrating vascular anatomical guidance into the masking strategy, VasoMIM compels the model to focus on sparse, semantically critical regions, thereby boosting the learning of vascular representations. Furthermore, the proposed anatomical consistency loss significantly enhances the discriminability of the learned representations. To facilitate large-scale pre-training, we have curated XA-170K, the largest X-ray angiogram dataset to date. Extensive experiments across six datasets, covering four distinct X-ray angiogram analysis tasks, demonstrate that VasoMIM achieves state-of-the-art performance. We believe this work offers a novel perspective on integrating anatomical knowledge into self-supervised learning, paving the way for the development of X-ray angiogram foundation models.

## REFERENCES

- [1] M. Vaduganathan, G. A. Mensah, J. V. Turco, V. Fuster, and G. A. Roth, “The global burden of cardiovascular diseases and risk: A compass for future health,” *JACC*, vol. 80, no. 25, pp. 2361–2371, 2022.
- [2] B. Kheiri, T. F. Simpson, M. Osman, D. M. German, C. S. Fuss, and M. Ferencik, “Computed tomography vs invasive coronary angiography in patients with suspected coronary artery disease: A meta-analysis,” *JACC: Cardiovasc. Imaging*, vol. 15, no. 12, pp. 2147–2149, 2022.
- [3] W. C. Members *et al.*, “2021 ACC/AHA/SCAI guideline for coronary artery revascularization: A report of the American College of Cardiology/American Heart Association Joint Committee on clinical practice guidelines,” *JACC*, vol. 79, no. 2, pp. e21–e129, 2022.
- [4] D.-X. Huang *et al.*, “Real-time 2D/3D registration via CNN regression and centroid alignment,” *IEEE TASE*, vol. 22, pp. 85–98, 2025.
- [5] D.-X. Huang *et al.*, “SPIRONet: Spatial-frequency learning and topological channel interaction network for vessel segmentation,” *arXiv*, 2024.
- [6] X. Li *et al.*, “STQD-Det: Spatio-temporal quantum diffusion model for real-time coronary stenosis detection in X-ray angiography,” *IEEE TPAMI*, vol. 46, no. 12, pp. 9908–9920, 2024.
- [7] S. Chen *et al.*, “Hierarchical heterogeneous aggregation network for multi-shape coronary stenosis detection in X-ray angiography sequences,” *IEEE TCSV*, 2025, DOI: [10.1109/TCSV.2025.3634766](https://doi.org/10.1109/TCSV.2025.3634766).

[8] A. Esteva *et al.*, “A guide to deep learning in healthcare,” *Nat. Med.*, vol. 25, no. 1, pp. 24–29, 2019.

[9] J. Gui *et al.*, “A survey on self-supervised learning: Algorithms, applications, and future trends,” *IEEE TPAMI*, vol. 46, no. 12, pp. 9052–9071, 2024.

[10] K. He, X. Chen, S. Xie, Y. Li, P. Dollár, and R. Girshick, “Masked autoencoders are scalable vision learners,” in *Proc. CVPR*, 2022, pp. 16 000–16 009.

[11] J. Zhuang *et al.*, “MiM: Mask in mask self-supervised pre-training for 3D medical image analysis,” *IEEE TMI*, 2025, DOI: [10.1109/TMI.2025.3564382](https://doi.org/10.1109/TMI.2025.3564382).

[12] F. Tang *et al.*, “MambaMIM: Pre-training Mamba with state space token interpolation and its application to medical image segmentation,” *Media*, p. 103606, 2025.

[13] H. Bao, L. Dong, S. Piao, and F. Wei, “BEiT: BERT pre-training of image transformers,” in *Proc. ICLR*, 2022.

[14] Z. Liu, J. Gui, and H. Luo, “Good helper is around you: Attention-driven masked image modeling,” in *Proc. AAAI*, vol. 37, no. 2, 2023, pp. 1799–1807.

[15] H. Wang *et al.*, “Bootstrap masked visual modeling via hard patch mining,” *IEEE TPAMI*, vol. 47, no. 8, pp. 6200–6214, 2025.

[16] J. Zhou *et al.*, “iBOT: Image BERT pre-training with online tokenizer” in *Proc. ICLR*, 2022.

[17] A. F. Frangi, W. J. Niessen, K. L. Vincken, and M. A. Viergever, “Multiscale vessel enhancement filtering,” in *Proc. MICCAI*, 1998, pp. 130–137.

[18] J. M. J. Valanarasu and V. M. Patel, “UNeXt: MLP-based rapid medical image segmentation network,” in *Proc. MICCAI*, 2022, pp. 23–33.

[19] L. Wu, J. Zhuang, and H. Chen, “Large-scale 3D medical image pre-training with geometric context priors,” *IEEE TPAMI*, 2025, DOI: [10.1109/TPAMI.2025.3639593](https://doi.org/10.1109/TPAMI.2025.3639593).

[20] Z. Qiu *et al.*, “Large-scale multi-sequence pretraining for generalizable MRI analysis in versatile clinical applications,” *arXiv*, 2025.

[21] F. Perez-Garcia *et al.*, “Exploring scalable medical image encoders beyond text supervision,” *Nat. Mach. Intell.*, vol. 7, no. 1, pp. 119–130, 2025.

[22] D.-X. Huang *et al.*, “VasoMIM: Vascular anatomy-aware masked image modeling for vessel segmentation,” in *Proc. AAAI*, 2026.

[23] X. Chen, S. Xie, and K. He, “An empirical study of training self-supervised vision transformers,” in *Proc. CVPR*, 2021, pp. 9640–9649.

[24] M. Caron *et al.*, “Emerging properties in self-supervised vision transformers,” in *Proc. ICCV*, 2021, pp. 9650–9660.

[25] Z. Xie *et al.*, “SimMIM: A simple framework for masked image modeling,” in *Proc. CVPR*, 2022, pp. 9653–9663.

[26] H.-Y. Zhou, S. Yu, C. Bian, Y. Hu, K. Ma, and Y. Zheng, “Comparing to learn: Surpassing ImageNet pretraining on radiographs by comparing image representations,” in *Proc. MICCAI*, 2020, pp. 398–407.

[27] K. Chaitanya, E. Erdil, N. Karani, and E. Konukoglu, “Contrastive learning of global and local features for medical image segmentation with limited annotations,” in *Proc. NeurIPS*, vol. 33, 2020, pp. 12 546–12 558.

[28] J. Yuan *et al.*, “HAP: Structure-aware masked image modeling for human-centric perception,” in *Proc. NeurIPS*, vol. 36, 2023, pp. 50 597–50 616.

[29] Q. Kang *et al.*, “Deblurring masked image modeling for ultrasound image analysis,” *Media*, vol. 97, p. 103256, 2024.

[30] C. Wang *et al.*, “Towards a general-purpose foundation model for fMRI analysis,” *arXiv*, 2025.

[31] H. Xu *et al.*, “A whole-slide foundation model for digital pathology from real-world data,” *Nature*, vol. 630, no. 8015, pp. 181–188, 2024.

[32] Y. Li, T. Luan, Y. Wu, S. Pan, Y. Chen, and X. Yang, “AnatoMask: Enhancing medical image segmentation with reconstruction-guided self-masking,” in *Proc. ECCV*, 2024, pp. 146–163.

[33] Z. Xu, Y. Liu, G. Xu, and T. Lukasiewicz, “Self-supervised medical image segmentation using deep reinforced adaptive masking,” *IEEE TMI*, vol. 44, no. 1, pp. 180–193, 2025.

[34] O. Ronneberger, P. Fischer, and T. Brox, “U-Net: Convolutional networks for biomedical image segmentation,” in *Proc. MICCAI*, 2015, pp. 234–241.

[35] S. Ren, K. He, R. Girshick, and J. Sun, “Faster R-CNN: Towards real-time object detection with region proposal networks,” *IEEE TPAMI*, vol. 39, no. 6, pp. 1137–1149, 2016.

[36] R.-Q. Li, G.-B. Bian, X.-H. Zhou, X. Xie, Z.-L. Ni, and Z.-G. Hou, “CAU-net: A novel convolutional neural network for coronary artery segmentation in digital subtraction angiography,” in *Proc. ICONIP*, 2020, pp. 185–196.

[37] D. Zhang *et al.*, “Direct quantification of coronary artery stenosis through hierarchical attentive multi-view learning,” *IEEE TMI*, vol. 39, no. 12, pp. 4322–4334, 2020.

[38] J. Chen *et al.*, “TransUNet: Rethinking the U-Net architecture design for medical image segmentation through the lens of transformers,” *Media*, vol. 97, p. 103280, 2024.

[39] J. Ruan, J. Li, and S. Xiang, “VM-UNet: Vision Mamba UNet for medical image segmentation,” *ACM TOMM*, 2024.

[40] J. Jiang *et al.*, “RWKV-UNet: Improving unet with long-range cooperation for effective medical image segmentation,” *arXiv*, 2025.

[41] M. Moor *et al.*, “Foundation models for generalist medical artificial intelligence,” *Nature*, vol. 616, no. 7956, pp. 259–265, 2023.

[42] C.-H. Wu *et al.*, “DeNvE-R: Deformable neural vessel representations for unsupervised video vessel segmentation,” in *Proc. CVPR*, 2025, pp. 15 682–15 692.

[43] R. Adams and L. Bischof, “Seeded region growing,” *IEEE TPAMI*, vol. 16, no. 6, pp. 641–647, 1994.

[44] H. Wang, Y. Tang, Y. Wang, J. Guo, Z.-H. Deng, and K. Han, “Masked image modeling with local multi-scale reconstruction,” in *Proc. CVPR*, 2023, pp. 2122–2131.

[45] M. Assran and other, “Self-supervised learning from images with a joint-embedding predictive architecture,” in *Proc. CVPR*, 2023, pp. 15 619–15 629.

[46] O. Siméoni *et al.*, “DINOv3,” *arXiv*, 2025.

[47] Z. Zhou, V. Sodha, J. Pang, M. B. Gotway, and J. Liang, “Models genesis,” *Media*, vol. 67, p. 101840, 2021.

[48] D. MH Nguyen *et al.*, “LVM-Med: Learning large-scale self-supervised vision models for medical imaging via second-order graph matching,” in *Proc. NeurIPS*, vol. 36, 2023, pp. 27 922–27 950.

[49] Y. Chu *et al.*, “Improving representation of high-frequency components for medical visual foundation models,” *IEEE TMI*, vol. 44, no. 8, pp. 3196–3209, 2025.

[50] Y. Yue, Y. Wang, C. Tao, P. Liu, S. Song, and G. Huang, “CheXWorld: Exploring image world modeling for radiograph representation learning,” in *Proc. CVPR*, 2025, pp. 20 778–20 788.

[51] Y. Li, Y. Wu, Y. Lai, M. Hu, and X. Yang, “MedDINOv3: How to adapt vision foundation models for medical image segmentation?” *arXiv*, 2025.

[52] A. Jiménez-Partinen *et al.*, “CADICA: A new dataset for coronary artery disease detection by using invasive coronary angiography,” *Expert Syst.*, vol. 41, no. 12, p. e13708, 2024.

[53] S. S. Mahmoudi *et al.*, “X-ray coronary angiogram images and SYNTAX score to develop machine-learning algorithms for CHD diagnosis,” *Sci. Data*, vol. 12, no. 1, p. 471, 2025.

[54] Y. Ma *et al.*, “Self-supervised vessel segmentation via adversarial learning,” in *Proc. ICCV*, 2021, pp. 7536–7545.

[55] I. Kruzhilov *et al.*, “CoronaryDominance: Angiogram dataset for coronary dominance classification,” *Sci. Data*, vol. 12, no. 1, p. 341, 2025.

[56] M. Popov *et al.*, “Dataset for automatic region-based coronary artery disease diagnostics using X-ray angiography images,” *Sci. Data*, vol. 11, no. 1, p. 20, 2024.

[57] V. V. Danilov *et al.*, “Real-time coronary artery stenosis detection based on modern neural networks,” *Sci. Rep.*, vol. 11, no. 1, p. 7582, 2021.

[58] A. Dosovitskiy *et al.*, “An image is worth 16x16 words: Transformers for image recognition at scale,” in *Proc. ICLR*, 2021.

[59] Y. Li, H. Mao, R. Girshick, and K. He, “Exploring plain vision transformer backbones for object detection,” in *Proc. ECCV*, 2022, pp. 280–296.

[60] N. Carion, F. Massa, G. Synnaeve, N. Usunier, A. Kirillov, and S. Zagoruyko, “End-to-end object detection with transformers,” in *Proc. ECCV*, 2020, pp. 213–229.

[61] T.-Y. Lin, P. Dollár, R. Girshick, K. He, B. Hariharan, and S. Belongie, “Feature pyramid networks for object detection,” in *Proc. CVPR*, 2017, pp. 2117–2125.

[62] S. Shit *et al.*, “clDice: A novel topology-preserving loss function for tubular structure segmentation,” in *Proc. CVPR*, 2021, pp. 16 560–16 569.

[63] A. Radford *et al.*, “Learning transferable visual models from natural language supervision,” in *Proc. ICML*, 2021, pp. 8748–8763.

[64] R. Zhang, P. Isola, A. A. Efros, E. Shechtman, and O. Wang, “The unreasonable effectiveness of deep features as a perceptual metric,” in *Proc. CVPR*, 2018, pp. 586–595.

[65] R. Mechrez, I. Talmi, and L. Zelnik-Manor, “The contextual loss for image transformation with non-aligned data,” in *Proc. ECCV*, 2018, pp. 768–783.

[66] L. v. d. Maaten and G. Hinton, “Visualizing data using t-SNE,” *JMLR*, vol. 9, no. Nov, pp. 2579–2605, 2008.